2023-09-20

A numerical study of the settling of non-spherical particles in quiescent water

Cheng, X

https://pearl.plymouth.ac.uk/handle/10026.1/21667

10.1063/5.0165555
Physics of Fluids
American Institute of Physics

A numerical study of the settling of non-spherical particles in quiescent water

Xiaoyong Cheng (程潇勇)[1], Zhixian Cao (曹志先)[1,a)], Ji Li (李季)[2], Alistair Borthwick[3,4]

AFFILIATIONS

[1]State Key Laboratory of Water Resources Engineering and Management, Wuhan University, Wuhan 430072, China

[2]Zienkiewicz Centre for Computational Engineering, Faculty of Science and Engineering, Swansea University, Swansea SA1 8EN, UK

[3]Institute for Infrastructure and Environment, The University of Edinburgh, Edinburgh EH9 3JL, UK

[4]School of Engineering, Computing and Mathematics, University of Plymouth, Plymouth PL4 8AA, UK

[a)]Author to whom correspondence should be addressed: zxcao@whu.edu.cn

ABSTRACT

The settling of non-spherical particles is poorly understood, with previous studies having focused mainly on spherical particles. Here, a series of particle-resolved direct numerical simulations are conducted using FLOW-3D (commercial computational fluid dynamics software) for spheres and five regular, non-spherical shapes of sediment particles, i.e., prolate spheroid, oblate spheroid, cylinder, disk, and cube. The Galileo number varies from 0.248 to 360 and the particle Reynolds number Re_p ranges from 0.00277 to 562. The results show that a non-spherical particle may experience larger drag and consequently attain a lower terminal velocity than an equivalent sphere. If Re_p is sufficiently small, the terminal velocity is less affected by particle shape as characterized by the particle aspect ratio. For relatively large Re_p, the shape effect (represented by the Corey shape factor) becomes more significant. Empirical correlations are derived for the dimensionless characteristic time t_{95*} and displacement s_{95*} of particle settling, which show that t_{95*} remains constant in the Stokes regime (Re_p < 1) and decreases with increasing Re_p in the intermediate regime (1 ≤ Re_p < 10^3), whereas s_{95*} increases progressively with increasing Re_p over the simulated range. It is also found that in the Stokes regime, particle orientation remains essentially unchanged during settling, and so the terminal velocity is governed by the initial orientation. In the intermediate regime, a particle provisionally settling at an unstable orientation self-readjusts to a stable equilibrium state, such that the effect of initial orientation on the terminal velocity is negligible. Moreover, an unstable initial orientation can enhance the vertical displacement and may promote vortex shedding.

HIGHLIGHTS

- Settling of non-spherical particles is investigated using commercial computational fluid dynamics software.
- At low particle Reynolds numbers, an increase in particle aspect ratio may correspond to a reduction in terminal velocity.
- The characteristic time remains constant throughout the Stokes regime and decreases with increasing particle Reynolds number in the intermediate regime.
- An unstable initial orientation may promote vortex shedding from particles settling in the intermediate regime.

I. INTRODUCTION

The settling of particles in fluids is key to many natural and industrial processes, such as sediment dynamics in alluvial rivers,[1,2] transportation of marine microplastics,[3,4] proppant settling in hydraulic fractures,[5,6] and chemical and powder processing.[7] Although particulate flows are generally turbulent and involve large amounts of particles, an improved understanding of the settling of a single particle in quiescent fluid is a prerequisite for modelling complex particle-laden turbulent flows. However, most existing models of particulate flows assume the grains to be spheres when in fact the most commonly encountered particles in practical applications are non-spherical.[8,9] Such simplification inevitably ignores the key roles played by particle shape and orientation in the settling process. Studies are urgently needed to gain better insight into the settling of non-spherical particles in quiescent water.

When a heavy particle falls through a static fluid, the particle accelerates due to gravity and increasing fluid drag is exerted on its surface. As the submerged weight of the particle is balanced by fluid drag, its acceleration terminates, enabling the particle to fall at a nearly constant velocity, called the terminal velocity. The drag force is one of the fundamental forces that affect the settling process, which can be defined as

$$F_d = \frac{1}{2} C_d \rho_f W^2 \frac{\pi}{4} d_n^{\,2}, \tag{1}$$

where C_d is the drag coefficient; ρ_f is the fluid density; W is the settling velocity; and d_n is the diameter of a sphere of equivalent volume to that of the particle. Accurate estimates of settling velocity and drag coefficient are of particular importance because other parameters can be readily inferred. Notably, the terminal velocity of a particle, denoted W_t, can be simply derived by equating the drag force to the submerged weight of the particle. The drag coefficient C_d in Eq. (1) is however very challenging to determine because it depends on many parameters including the particle Reynolds number and particle shape.[10] Herein, the particle Reynolds number is defined as $Re_p = Wd_n / \nu$, with ν being the kinematic viscosity. Except at sufficiently small Re_p, where an analytical solution exists for spheres based on Stokes' law, in which C_d is inversely proportional to Re_p, no general solution can be found for determining the drag coefficient of particles of any shape. Based on a large number of theoretical and experimental investigations of settling behavior, numerous empirical models have been developed to predict the drag coefficient and settling velocity of spherical particles[11-13] and non-spherical particles.[14-18] To account for the shape effect of non-spherical particles, various approaches have been proposed to define particle shape. Of these, the Corey shape factor[19] (CSF) is the most commonly used shape descriptor,[14,20,21] and is defined as $\mathrm{CSF} = d_s / \sqrt{d_m d_l}$, where d_s, d_m, and d_l are respectively the shortest, intermediate, and longest form dimensions of the particle. Sphericity ϕ is another widely used shape descriptor,[15,22,23] and is given by the ratio of the surface area of the volume-equivalent sphere to that of the actual particle. Circularity X is the ratio of the perimeter of the maximum projection area of the particle to the perimeter of a circle that has area equal to the maximum projection area. This descriptor is able to reflect the irregularity of particle contours and is thus very suitable for particles with sharp corners and large obtuse angles.[24] In addition, for highly irregular particles, the parameter ξ, which is the ratio ϕ / X, is another effective shape descriptor.[17,25,26] However, these aforementioned empirical models cannot provide sufficient effective information to quantify the whole process of particle settling. Consequently, the time and space scales that are required for a particle to reach its terminal settling state have not yet been resolved.

Particle orientation also has a vital effect on settling non-spherical particles. In general, a non-spherical particle could fall at any orientation without rotation at sufficiently small Re_p,[27,28] but will assume a stable orientation and tend to fall with the maximum projection area normal to the direction of settling motion at relatively large Re_p.[8,29] Besides, particle orientation can appreciably modify the drag coefficient.[16,18] Over the past decade, particle-resolved direct numerical simulation (PR-DNS) has been carried out to establish correlations between C_d and particle orientation.[30-33] However, such correlations are based on the assumption of a stationary obstacle exposed to a moving fluid, therefore neglecting the effects of secondary motions and wake structures.[34] Moreover, most existing numerical studies considering the influence of particle orientation on free settling have been confined to two-dimensional modeling.[35-37] Overall, there is a need for a three-dimensional model that can properly address the effect of particle orientation on the settling process of non-spherical particles.

The present work sets out to unravel the effects of particle shape and initial orientation on the settling of non-spherical sediment particles in quiescent water. Using the commercial computational fluid dynamics (CFD) software FLOW-3D (version 11.2), a series of PR-DNS simulations are performed for a range of particle sizes, shapes, and distinct initial orientations. Based on the computational results, key parameters that characterize the settling process, including terminal velocity W_t and drag coefficient C_d, are analyzed to reveal the influence of particle shape on settling. Furthermore, the time and space scales required to reach terminal settling are also investigated. In addition, the settling processes of non-spherical particles in the Stokes and intermediate regimes are presented, thereby probing into the effect of initial particle orientation.

II. METHOD

A. Computational fluid dynamics (CFD) model

The commercial CFD software FLOW-3D, developed by Flow Science, is used to conduct PR-DNS simulations of particle settling in otherwise quiescent fluid. FLOW-3D utilizes a fractional area/volume obstacle representation (FAVOR) technique[38] and provides a general moving object model that can simulate rigid body motion that is dynamically coupled with fluid flow. The FAVOR method defines complicated geometric shapes through fractional areas and volumes within rectangular elements and has proven to be one of the most efficient methods to treat immersed solid bodies.[39,40]

Assuming the fluid to be incompressible, the continuity and momentum equations based on the FAVOR method are given as

$$\frac{\partial U_i}{\partial x_i} = -\frac{\partial V_f}{\partial t}, \tag{2}$$

$$\frac{\partial u_i}{\partial t} + \frac{U_j}{V_f}\frac{\partial u_i}{\partial x_j} = -\frac{1}{\rho_f}\frac{\partial p}{\partial x_i} + g_i + f_i, \tag{3}$$

where subscripts i and $j = 1,2,3$ denote x, y, and z directions; x_i are Cartesian coordinates; t is time; $U_i = u_i A_i = \left(uA_x, vA_y, wA_z\right)$ in which u_i is the i-th velocity component and A_i is the corresponding area fraction; V_f is volume fraction; p is pressure; g_i is the i-th body acceleration component; and f_i is the i-th viscous acceleration component. The viscous acceleration components in Eq. (3) are calculated as

$$f_i = \frac{1}{\rho_f V_f}\left(wsx_i - \frac{\partial T_{ij}}{\partial x_j} \right), \tag{4}$$

where wsx_i are wall shear stress components; and $T_{ij} = A_{\underline{j}}\tau_{ij} = -2A_{\underline{j}}\mu\left(s_{ij} - s_{kk}\delta_{ij}/3\right)$, in which μ is dynamic viscosity, $s_{ij} = \left(\partial u_i/\partial x_j + \partial u_j/\partial x_i\right)/2$ is the strain rate tensor, and δ_{ij} is the Kronecker delta function. Compared to the continuity equation applied in stationary obstacle problems, $-\partial V_f/\partial t$ on the right-hand side of Eq. (2) is equivalent to an additional volume source term and exists solely in mesh cells around the boundary of the moving object. The term is evaluated as

$$-\frac{\partial V_f}{\partial t} = \frac{S_{\text{obj}}}{V_{\text{cell}}} V_{\text{obj}i} n_i, \tag{5}$$

where V_{cell} is the volume of a mesh cell; S_{obj}, n_i, and $V_{\text{obj}i}$ are respectively the surface area, unit normal vector, and velocity of the moving object in the mesh cell.

According to kinematics, the general motion of a rigid body can be divided into translational motion and rotational motion components. Newton's second law describes the translational motion of a rigid body as

$$m_p \frac{d\mathbf{V}_G}{dt} = \mathbf{F}, \tag{6}$$

where $\mathbf{V}_G$ is the mass center velocity of the rigid body; $\mathbf{F}$ is the total force on the body; and m_p is rigid body mass. Euler's equation describes rigid body rotation in a frame of reference fixed at the centroid of the rotating body as

$$\mathbf{I}\frac{d\boldsymbol{\omega}}{dt} + \boldsymbol{\omega} \times \left(\mathbf{I}\boldsymbol{\omega}\right) = \mathbf{T}_G, \tag{7}$$

where $\boldsymbol{\omega}$ is the angular velocity of the rigid body; $\mathbf{I}$ is the diagonal inertia matrix relative to the principal axes of the rigid body; and $\mathbf{T}_G$ is the total torque about the mass center. The present paper considers the free settling of a single particle, so the total force and total torque include only hydrodynamic and gravitational forces and torques.

The CFD model solves the governing equations of fluid motion [Eqs. (2) and (3)] using a finite volume/finite difference method.[41] Pressures and velocities are coupled implicitly and solved by using a generalized minimal residual method, which is the default solver of FLOW-3D. The momentum advection algorithm adopts a first-order upwind scheme. For coupled rigid body motion [Eqs. (6) and (7)], both the explicit and implicit general moving objects methods work well since heavy object problems are considered in the present paper.

B. Study cases

A series of numerical cases are used to investigate the influences of particle shape and initial orientation on the settling of non-spherical particles. Table I summarizes the simulation parameters. In all cases, the fluid is specified as water at 20 °C (ρ_f = 1000 kg/m^3, ν = 1×10^{-6} m^2/s), and the particles are assumed to be composed of siliciclastic sediment of homogeneous density 2650 kg/m^3. Eight spherical equivalent diameters are considered, i.e., d_n = 0.015625, 0.03125, 0.0625, 0.125, 0.25, 0.5, 1, and 2 mm. Consequently, the value of the Galileo number varies from 0.248 to 360. The Galileo number Ga is the ratio between gravitational and viscous forces, and is defined as

$$Ga = \frac{\sqrt{\left|\rho_p / \rho_f - 1\right| g d_n^{\,3}}}{\nu}, \tag{8}$$

where ρ_p is particle density; and g is gravitational acceleration. As indicated in Table II, six particle shapes are considered, including spheres and five regular non-spherical shapes, i.e., prolate spheroid, oblate spheroid, cylinder, disk, and cube, with the first four shapes being axisymmetric. Although particles in natural and industrial processes are generally irregular, it is justified to choose regular non-spherical particles as the object of the present study because most accurate models for predicting the behavior of non-spherical particles in fluids have been based on studies on regular particles, for which the characterization of the particle shape is not complex.[18]

Among the parameters listed in Table I, β is defined as the angle between the plane in which the maximum projection area of a particle lies and the horizontal plane perpendicular to the direction of settling motion (and thus provides a reasonable description of the particle orientation). β_0 denotes the initial orientation of a particle upon release. As previously noted, a particle settling at sufficiently small Re_p exhibits no preferred orientation. If Re_p is relatively large, a particle tends to fall with its maximum projection area normal to the direction of settling motion, i.e., at a state of $\beta = 0°$. Therefore, the typical initial state of $\beta_0 = 0°$ is chosen to exclude any influence of orientation variation; the combination of different particle sizes and shapes leads to 36 cases. A further 32 cases that consider two distinct initial orientations ($\beta_0 = 45°$ and $90°$) are simulated for axisymmetric particles with four selected spherical equivalent diameters (d_n = 0.015625, 0.0625, 0.25, and 1 mm). Overall, a total of 68 numerical cases are considered, and the particle Reynolds number Re_p ranges from 0.00277 to 562, covering both the Stokes regime ($Re_p < 1$) and the intermediate regime ($1 \leq Re_p < 10^3$).

In this paper, the Corey shape factor CSF is used to describe particle shape, noting that CSF suffices for regular particles.[42] The projection area protocol, which is associated with the lowest operator-dependent errors compared to other methods,[43] is applied to determine the form dimensions of a given particle (see Table II). Particle settling is simulated in a domain of dimensions $8d_n \times 8d_n$ in the *x* and *y* directions. The size of the domain in the *z*-direction is carefully determined to ensure the whole-process modeling of particle settling can be achieved without exceptional computational cost. A resolution of 12 grids per d_n is used, which can successfully resolve the geometry of both spherical and non-spherical particles considered in the present study. Periodic boundary conditions are imposed in the horizontal directions to mimic an unbounded domain without wall effect, and a free surface and a stationary wall are implemented at the upper and bottom boundaries. More information on validation of the CFD model is given in the Appendix. In addition, a dual-Euler whole-attitude solver is used to reproduce the variation in orientation of particles, based on the time series of particle angular velocities output from the CFD model. A brief description of the method is given in the Supplementary Material.

TABLE I. Summary of simulation parameters.

ρ_f $\left(\mathrm{kg/m^3}\right)$	ν $\left(\mathrm{m^2/s}\right)$	ρ_p $\left(\mathrm{kg/m^3}\right)$	d_n (mm)	β_0 $(°)$
1000	1×10^{-6}	2650	0.015625-2	0, 45 and 90

TABLE II. Summary of six particle shapes considered in this work. Semi-axes lengths of the ellipsoid are a, b, and c; the diameter and height of the cylinder and disk are d and h ($d < h$ for the cylinder, $d > h$ for the disk), respectively; and the edge length of the cube is a.

Shape	d_l	d_m	d_s	CSF
Sphere	d_n	d_n	d_n	1.00
Ellipsoid 1 (prolate spheroid, $a = 4b = 4c$)	$2a$	$2b$	$2c$	0.50
Ellipsoid 2 (oblate spheroid, $a = b = 2c$)	$2a$	$2b$	$2c$	0.50
Cylinder ($h = 2d$)	$\sqrt{h^2 + d^2}$	d	d	0.67
Disk ($h = 1/4d$)	$\sqrt{h^2 + d^2}$	d	h	0.25
Cube	$\sqrt{3}a$	$\sqrt{2}a$	a	0.64

III. RESULTS AND DISCUSSION

A. Particle settling with maximum projection area normal to fall direction

1. Terminal settling state

The terminal settling state and terminal velocity of a particle are simultaneously attained when the submerged weight of the particle is balanced by fluid drag. Terminal velocity is a fundamental hydrodynamic parameter that both directly and indirectly governs sedimentary processes.[29] Here, the terminal velocity W_t and spherical equivalent diameter d_n are normalized following Dietrich[14], such that:

$$W_{t*} = \frac{\rho_f W_t^3}{\left(\rho_s - \rho_f\right) g\nu}, \tag{9}$$

$$d_* = \frac{\left(\rho_s - \rho_f\right) g d_n^{\ 3}}{\rho_f \nu^2}, \tag{10}$$

where W_{t*} is the dimensionless terminal velocity; and d_* is the dimensionless spherical equivalent diameter. Figure 1 illustrates the variation in W_{t*} with d_* obtained for different shapes when $\beta_0 = 0°$. It appears that a non-spherical particle attains a lower terminal velocity than its spherical counterpart, with the difference in terminal velocity becoming increasingly evident as the particle size increases. This trend is further confirmed in Figure 2 which shows the variation in δ with particle Reynolds number Re_p where δ is defined as the relative deviation of the terminal velocity of a non-spherical particle from that of its spherical counterpart with the same d_n as follows:

$$\delta = \frac{W_t - W_{t-\text{sphere}}}{W_{t-\text{sphere}}} \times 100\%. \tag{11}$$

For a specific non-spherical particle shape, δ remains essentially unchanged in the

Stokes regime, whereas δ decreases progressively with increasing Re_p in the intermediate regime. Fig. 2 also shows that δ varies with particle shape. In addition to the CSF, the aspect ratio obtained by dividing d_l by d_s is selected here to account for the shape effect. In the Stokes regime with low Re_p, δ is largely dependent on aspect ratio, with larger particle aspect ratio corresponding to smaller terminal velocity. The foregoing observations indicate that the longest and shortest form dimensions may govern terminal velocity in the Stokes regime. Therefore, elongated, flat particles may reach almost equal values of terminal velocity despite their distinct shapes. When Re_p exceeds 10, the computed δ generally decreases with decreasing CSF, and little consistency is observed between δ and the aspect ratio. In short, when the viscous force dominates, the terminal velocity is less affected by the non-spherical particle shape, which can be characterized by the particle aspect ratio. When the inertial force becomes dominant, the shape effect tends to become significant, and should be represented by CSF instead of aspect ratio.

Figure 3 illustrates the drag coefficient C_d as a function of particle Reynolds number Re_p. Results obtained from the spherical drag law proposed by Clift and Gauvin[11] are also included for comparison. The computed C_d curve for spheres exhibits satisfactory agreement with Clift and Gauvin's empirical relationship, confirming the validity of the present model. Non-spherical particles are predicted to experience relatively larger drag than equivalent spheres, with the difference between drag coefficient values progressively increasing as Re_p increases.

When a particle moves through a fluid, the total drag exerted on its surface can be divided into pressure drag (or form drag) F_{pd} and friction drag F_{fd}. We consider the drag ratio F_{fd}/F_{pd} which is defined as the ratio between friction drag and pressure drag of a particle at the terminal settling state. Figure 4 illustrates the dependency of the drag ratio F_{fd}/F_{pd} on particle Reynolds number Re_p. The computed F_{fd}/F_{pd} of spheres settling in the Stokes regime is approximately 2, close to the theoretically derived value.[2] Moreover, the computed F_{fd}/F_{pd} of a specific shape remains constant throughout the Stokes regime and gradually decreases as Re_p increases in the intermediate regime. For given Re_p, the value of F_{fd}/F_{pd} generally increases with increasing CSF. These results suggest that when the inertial force becomes significant or the particle shape deviates from spherical, pressure drag gradually dominates over friction drag.

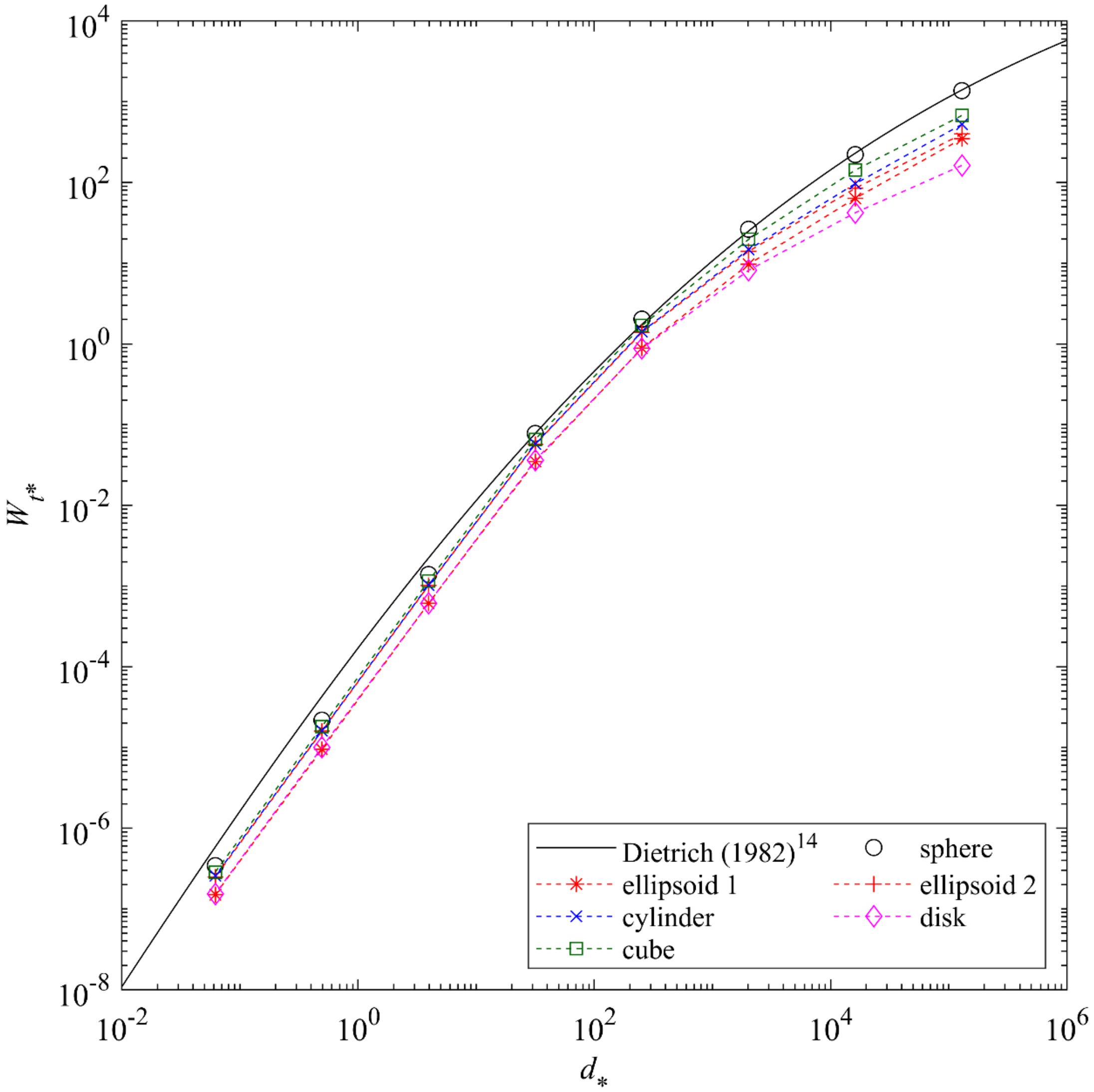

FIG. 1. Dimensionless terminal velocity W_{t*} against dimensionless spherical equivalent diameter d_* obtained for different particle shapes when $\beta_0 = 0°$. Solid line refers to the model by Dietrich[14].

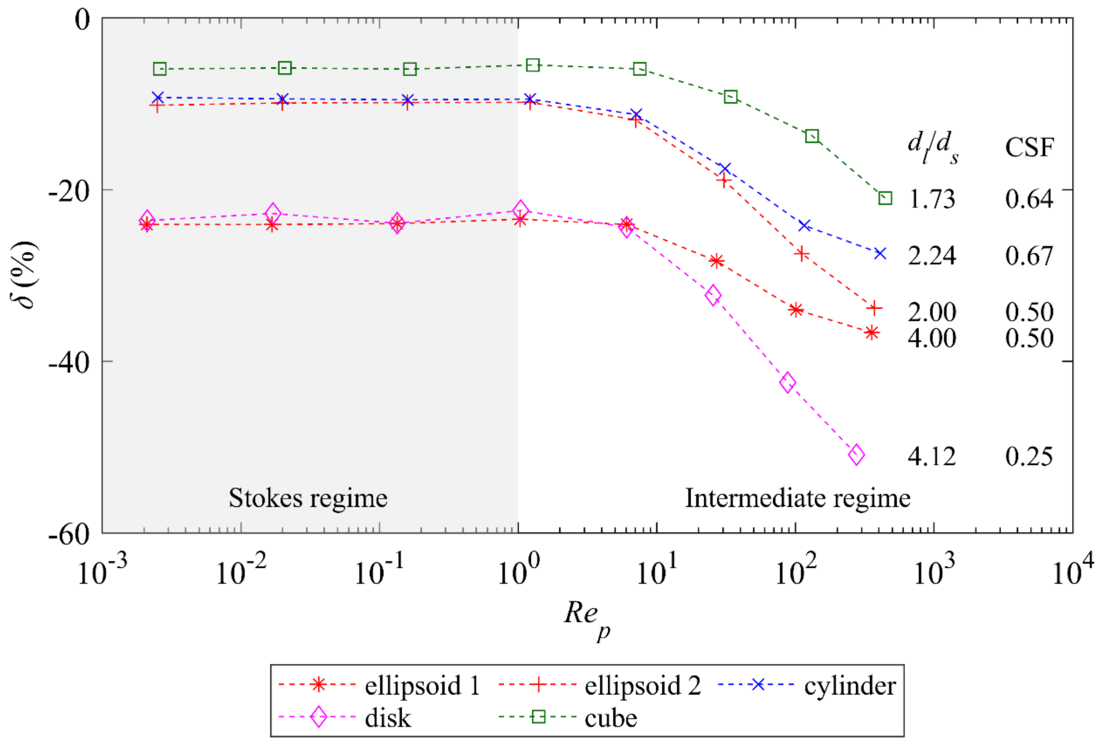

FIG. 2. Predicted dependence of relative deviation δ in terminal velocity of a non-spherical particle to that of a sphere of the same equivalent diameter on particle Reynolds number Re_p.

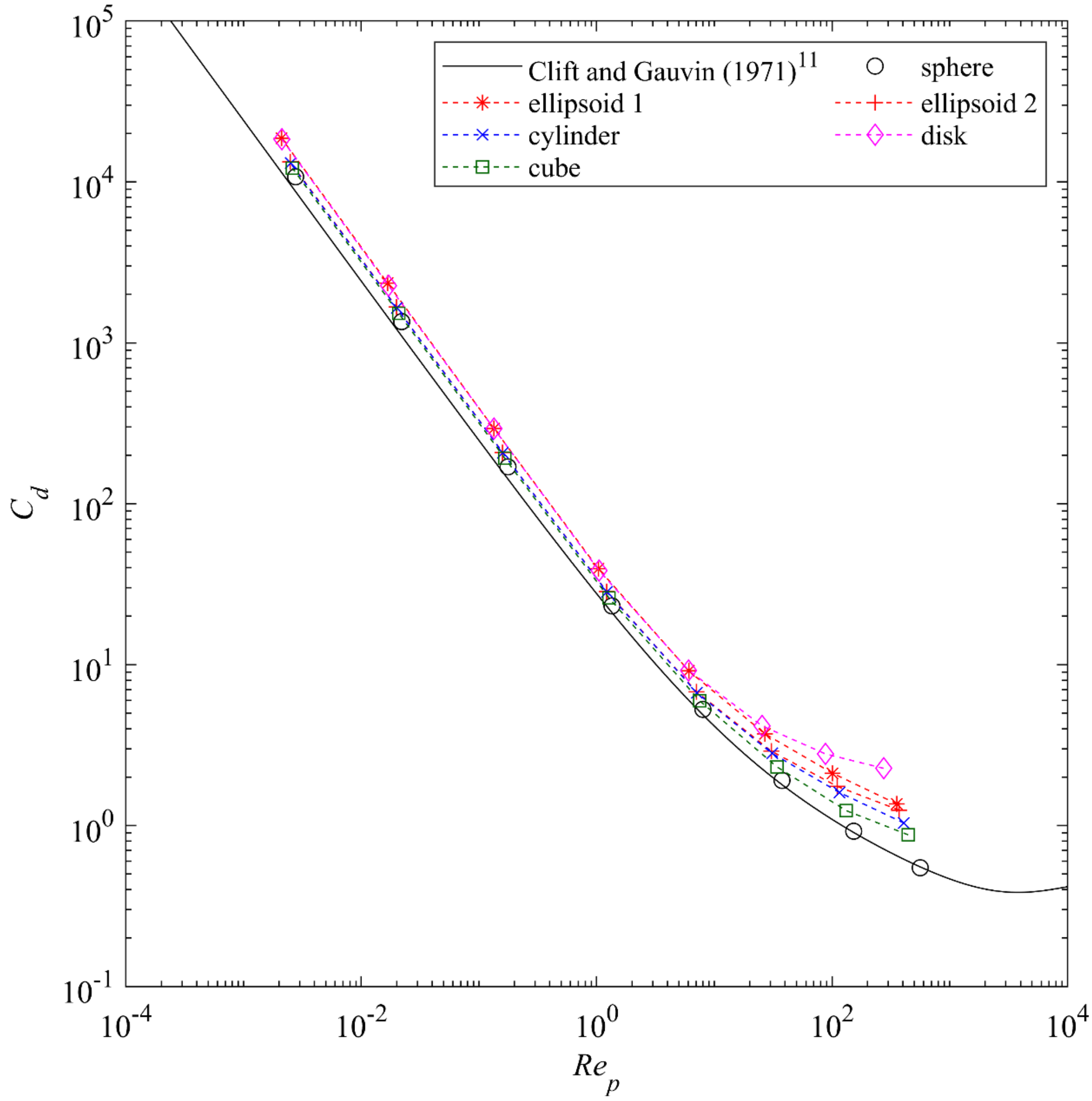

FIG. 3. Dependence of predicted drag coefficient C_d on particle Reynolds number Re_p. Solid line is the spherical drag law proposed by Clift and Gauvin[11].

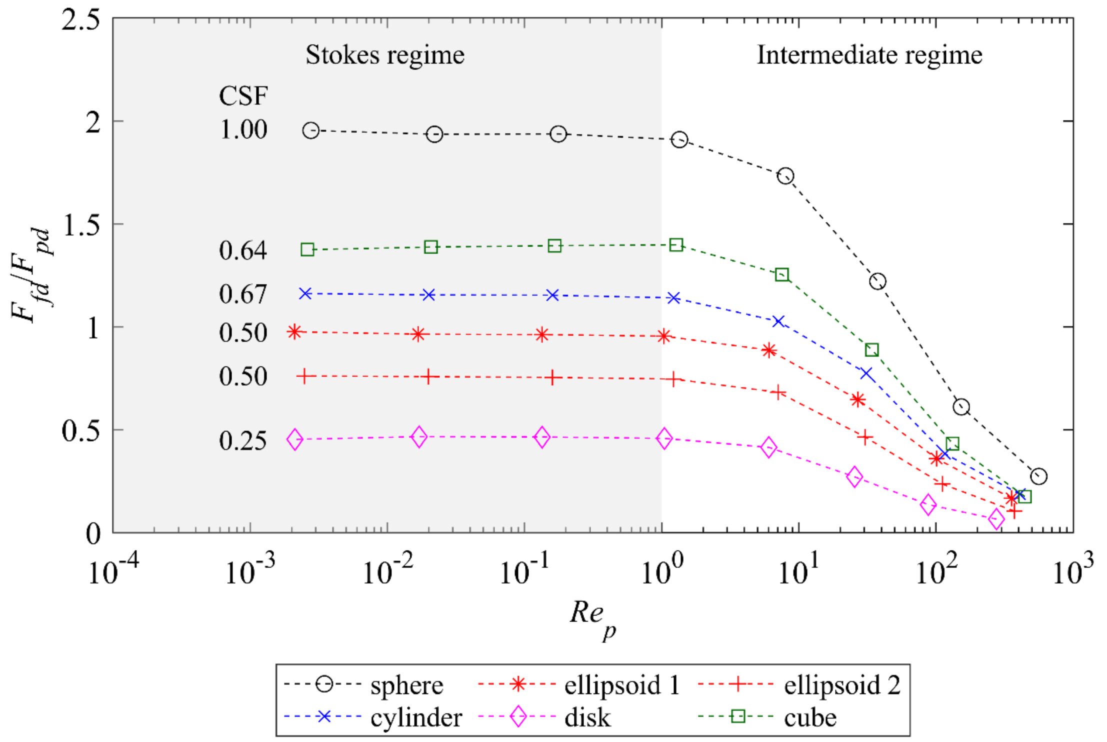

FIG. 4. Predicted dependence of drag ratio F_{fd} / F_{pd} on particle Reynolds number Re_p.

2. *Characteristic time and displacement*

Although the settling velocity and drag coefficient have been extensively studied for both spherical and non-spherical particles, limited attention has been paid to the time and space scales required for a particle to reach its terminal settling state.

The motion of a spherical particle falling through a fluid is described theoretically by the Boussinesq-Basset-Oseen equation,[2] expressed as

$$\left(m_p+\alpha_m m_f\right)\frac{dW}{dt}=(m_p-m_f)g-F_d-\frac{3}{2}d_n^{\,2}\left(\pi\rho_f\mu\right)^{1/2}\int_0^t\frac{dW}{d\sigma}\frac{d\sigma}{(t-\sigma)^{1/2}},\qquad(12)$$

where m_f is the mass of fluid displaced by the sphere; α_m is the added mass coefficient; and σ is a dummy variable. In Eq. (12), the term on the left-hand side denotes particle inertia, and includes the added mass effect when an accelerating (or retarding) particle moves in a fluid. In practice, it is common to assume $\alpha_m = 0.5$. On the right-hand side of Eq. (12), the first term is the submerged weight of the particle, the second term represents the fluid drag, and the third term is the Basset force (due to particle acceleration because of unsteady viscous shear on the surface of the particle).

Guo[44] derived a simple closed-form solution for the motion of a sphere settling through a fluid by applying Rubey's drag law[45] to Eq. (12) and combining the added mass and the Basset force into an integrated term. Guo was able to determine analytically the time-dependent settling velocity, acceleration, and vertical displacement of a spherical particle. However, for a non-spherical particle, even when the orientation variation is neglected and the drag force approximated by an empirical relationship, it is extremely difficult to obtain analytical solutions for the added mass and the Basset force. In practice, empirical relations have to be introduced in order to describe the characteristic time and characteristic displacement of a settling non-spherical particle.

Here, we focus on cases with $\beta_0 = 0°$, where particles accelerate to the terminal settling state with negligible change in orientation. The characteristic time t_{95} and characteristic displacement s_{95} are defined as the time and vertical displacement taken for a particle to reach 95% of its terminal velocity. A general dimensional analysis gives the following expressions:

$$t_{95*} = \frac{t_{95}}{d_n^{\ 2} / \nu} = f_1\left(Re_p\right), \tag{13}$$

$$s_{95*} = \frac{s_{95}}{d_n} = f_2\left(Re_p\right), \tag{14}$$

where t_{95*} and s_{95*} are dimensionless characteristic time and displacement. Figure 5 depicts the behavior of t_{95*} and s_{95*} with Re_p, as logarithmic plots. Linear fitting is used to obtain two asymptotes for the Stokes and intermediate regimes, with their intersection set at $Re_p = 1$. As shown in Fig. 5(a), the dimensionless characteristic time t_{95*} is assumed constant throughout much of the Stokes regime, and then decreases with increasing Re_p in the intermediate regime. The dimensionless characteristic displacement s_{95*} increases monotonically with increasing Re_p over the simulated range, with the linear slope observed in the Stokes regime reducing in the intermediate regime [Fig. 5(b)]. These results suggest that the Stokes and intermediate regimes are characterized by two distinct acceleration mechanisms. Based on the two asymptotes, the logarithmic matching approach proposed by Guo[46] is used to establish the following correlation formulae:

$$t_{95*} = 2.226\left(1 + Re_p^{\ 3.126}\right)^{-0.222}, \tag{15}$$

$$s_{95*} = 1.716 Re_p^{\ 0.998}\left(1 + Re_p^{\ 3.409}\right)^{-0.209}. \tag{16}$$

The above correlations are evaluated using the coefficient of determination R^2 and mean relative error MRE, which are defined as

$$\mathrm{R}^2 = 1 - \frac{\sum_{k=1}^{N}\left(\eta_k^{\mathrm{cal}} - \eta_k^{\mathrm{sim}}\right)^2}{\sum_{k=1}^{N}\left(\overline{\eta^{\mathrm{sim}}} - \eta_k^{\mathrm{sim}}\right)^2}, \tag{17}$$

$$\mathrm{MRE} = \frac{1}{N}\sum_{k=1}^{N}\left|\frac{\eta_k^{\mathrm{cal}} - \eta_k^{\mathrm{sim}}}{\eta_k^{\mathrm{sim}}}\right|, \tag{18}$$

where η_k^{cal} is the *k*-th data value obtained from the correlation functions; η_k^{sim} is the *k*-th data value from the numerical simulations; $\overline{\eta^{\mathrm{sim}}}$ is the mean value of the simulated data; and N is the number of pairs of data points. In general, higher R^2 and lower MRE correspond to better model performance. As demonstrated in Table III, our theoretical model exhibits rather good performance with high R^2 and acceptable MRE. The proposed correlations indicate that the time and space scales required for a non-spherical particle to reach its terminal settling state may vary with Re_p, and provide convenient methods that give effective estimates of the magnitudes of the characteristic time and displacement. It should be noted that the proposed correlations are only valid within the simulated range of Re_p for a particle-to-fluid density ratio ρ_p / ρ_f of 2.65. Future work will be extended to the Newton regime ($Re_p > 10^3$) and incorporate a larger range of density ratios.

TABLE III. Performance of proposed correlation formulae Eq. (15) for dimensionless characteristic time and Eq. (16) for dimensionless characteristic displacement against underlying simulated data.

Correlation	R^2	MRE (%)
Eq. (15)	0.9971	5.948
Eq. (16)	0.9988	3.453

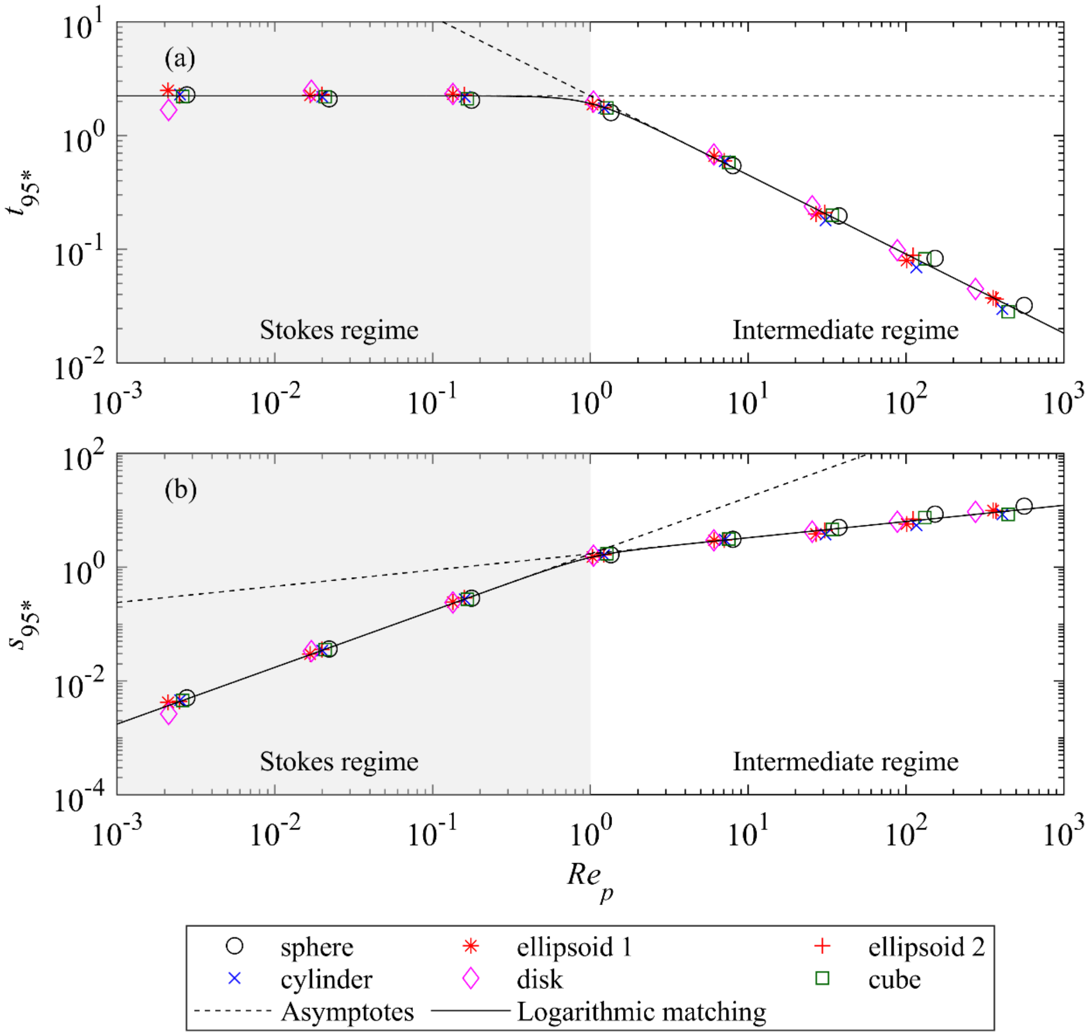

FIG. 5. Dependence on particle Reynolds number Re_p of (a) dimensionless characteristic time t_{95*} and (b) dimensionless characteristic displacement s_{95*}.

B. Particle settling for different initial orientations.

1. Stokes regime

In this section, results from numerical cases with $d_n = 0.0625$ mm and Re_p ranging from 0.1 to 0.2 are analyzed to investigate the effect of initial orientation on the settling of non-spherical particles in the Stokes regime. Note that similar results are found for cases with $d_n = 0.015625$ mm and $2\times10^{-3} < Re_p < 3\times10^{-3}$, and so are not included here.

Taking ellipsoid 1 as an example, Fig. 6 shows the temporal variations in orientation angle β, settling velocity W, and vertical displacement s. It can be seen that β remains constant during the settling process for cases with different β_0 [Fig. 6(a)]. This suggests that the orientation remains essentially unchanged for non-spherical particles settling in the Stokes regime, in agreement with previous findings.[27,28] As a result, a non-spherical particle reaches a terminal velocity that depends on the initial orientation of the particle [Fig. 6(b)]. And particles with larger β_0 tend to settle faster, yielding longer vertical displacements [Fig. 6(c)].

To account for the effect of particle orientation, we consider crosswise sphericity ϕ_c, which is the ratio between the cross-sectional area of a volume-equivalent sphere and the projection area of the actual particle perpendicular to the flow.[16] According to the definition of β, particles with large β should have relatively small projection areas and consequently develop large ϕ_c.

Figure 7 illustrates the influence of particle orientation on terminal settling state by showing the resulting variations in terminal velocity W_t and drag ratio F_{fd} / F_{pd} with ϕ_c. In general, larger ϕ_c leads to larger W_t, indicating that the particle experiences lower total drag at larger β. In addition, F_{fd} / F_{pd} tends to increase as ϕ_c increases, implying that the contribution from friction drag may increase despite reduction in total drag when the particle is oriented away from $\beta = 0°$. Figure 8 presents contour plots of vertical flow velocity in the vicinity of particles of different shapes and initial orientation $\beta_0 = 45°$ at the terminal settling state. Cases with $\beta_0 = 45°$ are of particular interest because the particles display asymmetric forms in the vertical plane. As shown in Fig. 8, the velocity contours exhibit a highly symmetric pattern and turn out to be similar for different particle shapes. The particles seem to move in combination with the surrounding fluid, and so the effect of asymmetry of the solid shape is marginal. Arguably, this accounts for the sustainability of random orientations.

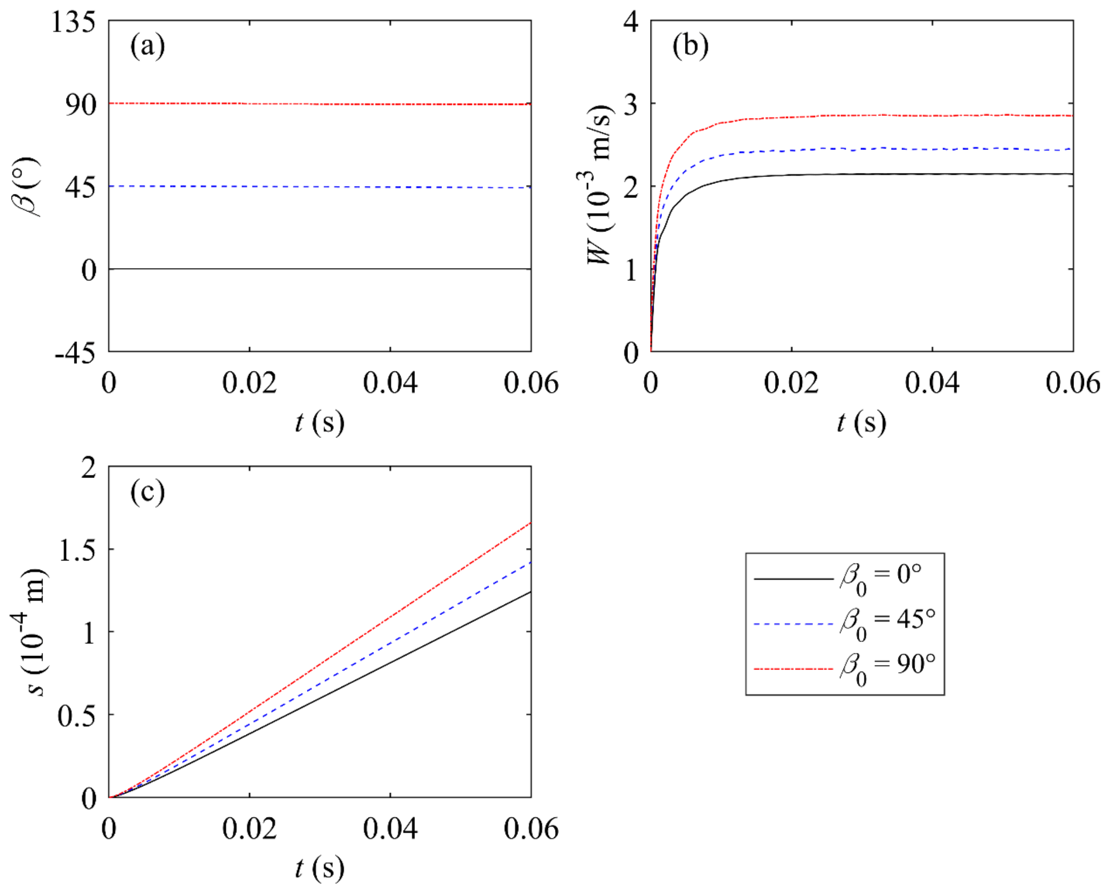

FIG. 6. Time histories of (a) orientation angle β, (b) settling velocity W, and (c)

vertical displacement s for ellipsoid 1 with $d_n = 0.0625$ mm.

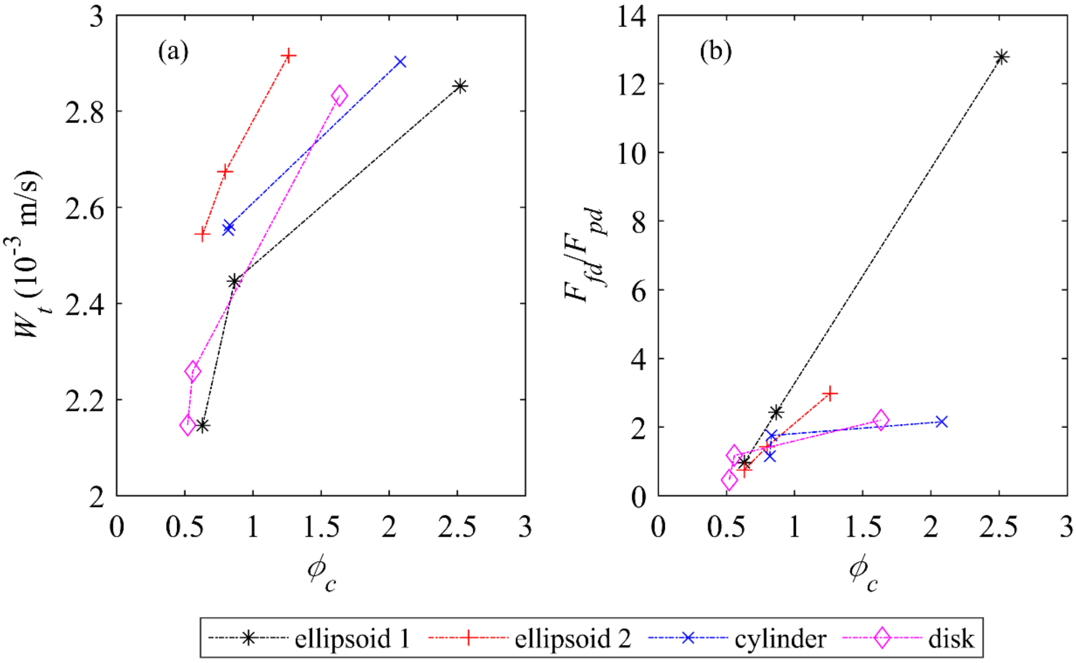

FIG. 7. Predicted dependencies of (a) terminal velocity W_t and (b) drag ratio F_{fd} / F_{pd} on crosswise sphericity ϕ_c for particles of different shapes with $d_n = 0.0625$ mm.

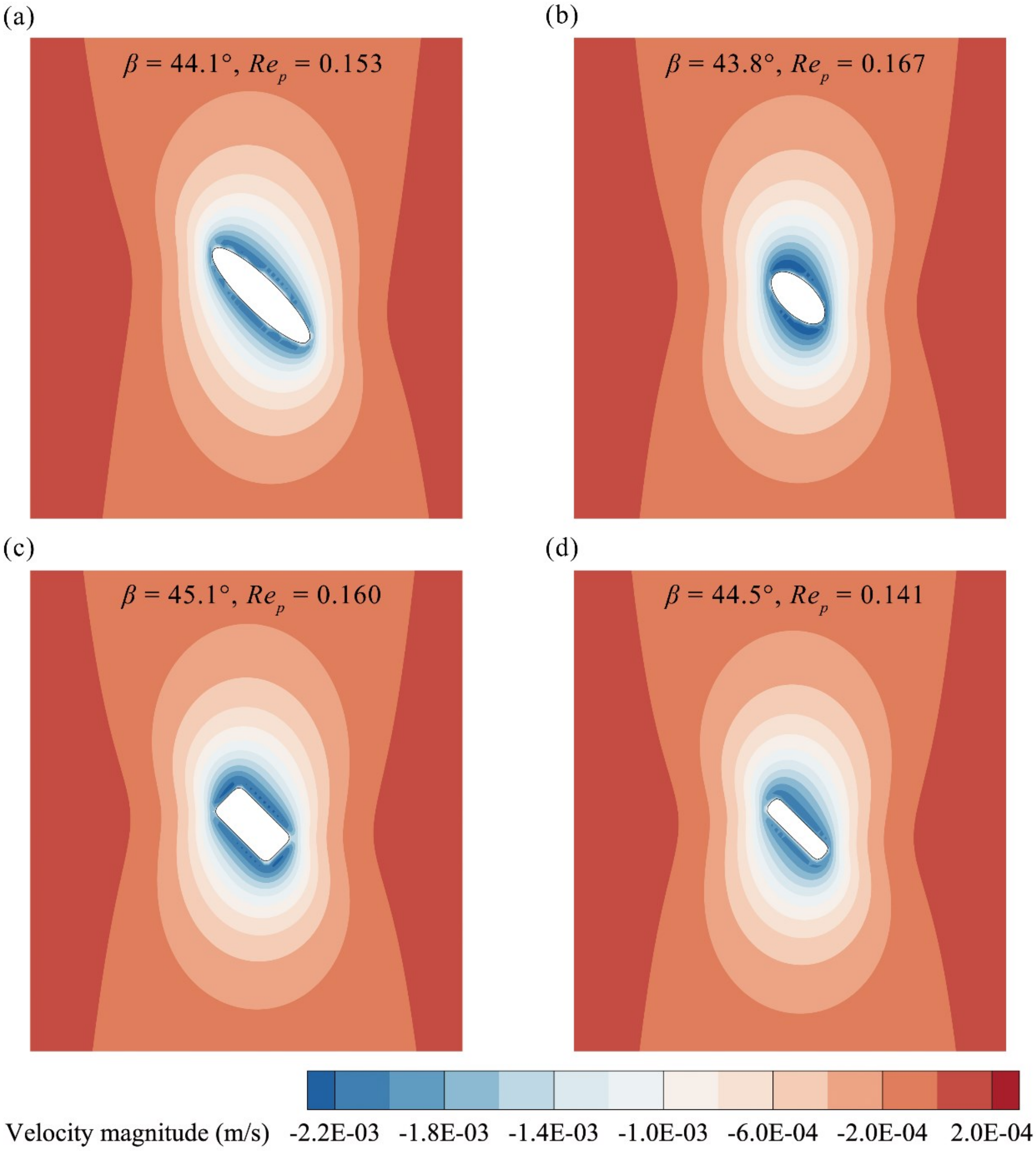

FIG. 8. Contour plots of vertical flow velocity around differently shaped particles with $d_n = 0.0625$ mm and $\beta_0 = 45°$ at the terminal settling state ($t = 0.06$ s): (a) ellipsoid 1, (b) ellipsoid 2, (c) cylinder, and (d) disk.

2. Intermediate regime

Here numerical cases with $d_n = 1$ mm and $Re_p \approx 100$ are selected to probe into the effect of initial orientation on the settling of non-spherical particles in the intermediate regime. As can be seen from Fig. 9(a), particles of ellipsoid 1 shape tend to attain the same terminal settling state with $\beta = 0°$ irrespective of their initial orientation, consistent with the previously mentioned settling behavior at relatively large Re_p.[8,29] Variation in particle orientation has a vital effect on the settling process, about which more details are given later in this section. Yet, due to the identical orientation attained at terminal settling, the effect of initial orientation on terminal velocity can be negligible [see Fig. 9(b)]. Except for the disk, similar results have been found for other particle shapes. At the terminal settling state, periodic oscillations about $\beta = 0°$ are observed for the disk particle [Figs. 9(d) and 9(e)]. Such results are in accordance with previous observations by Stringham et al.[47] at a higher value of Re_p.

Fig. 10 depicts two-dimensional visualizations of the settling trajectory and orientation variation of different particles with $\beta_0 = 90°$. The red dashed line denotes the centroid trajectory and the black solid line with blue endpoints denotes the location of the revolution axis. The time increment between each visualization is 0.02 s. During the settling process, the revolution axes of elongated particles (ellipsoid 1 and the cylinder) become gradually oriented normal to the direction of settling motion, while those of flat particles (ellipsoid 2 and the disk) turn to be parallel to the settling direction, thus the $\beta = 0°$ state is eventually reached. In addition to the vertical fall, a horizontal component can be observed in the settling path, associated with the varying orientation.

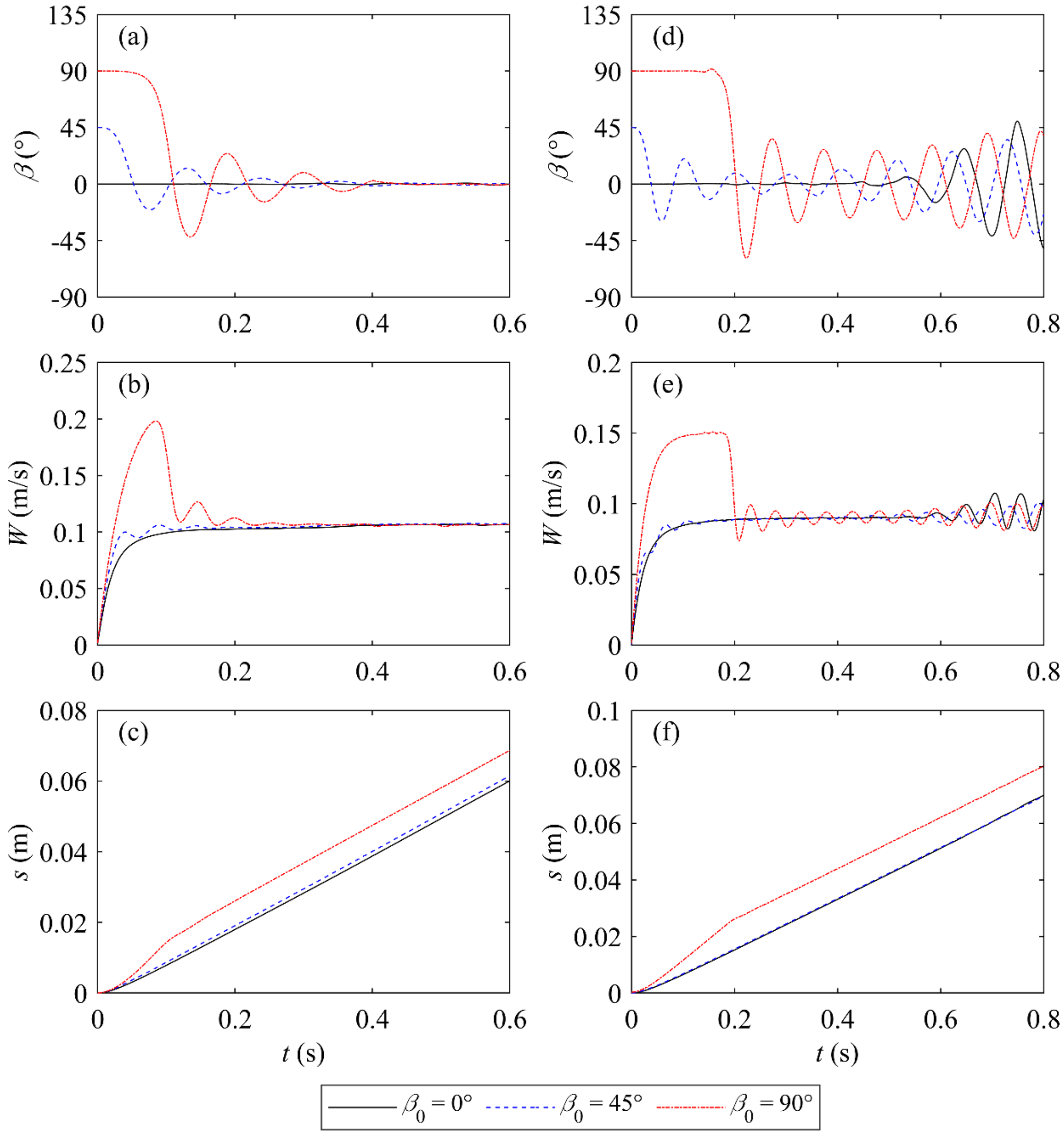

FIG. 9. Time histories of orientation angle β, settling velocity W, and vertical displacement s for (a-c) ellipsoid 1 and (d-f) disk with $d_n = 1$ mm.

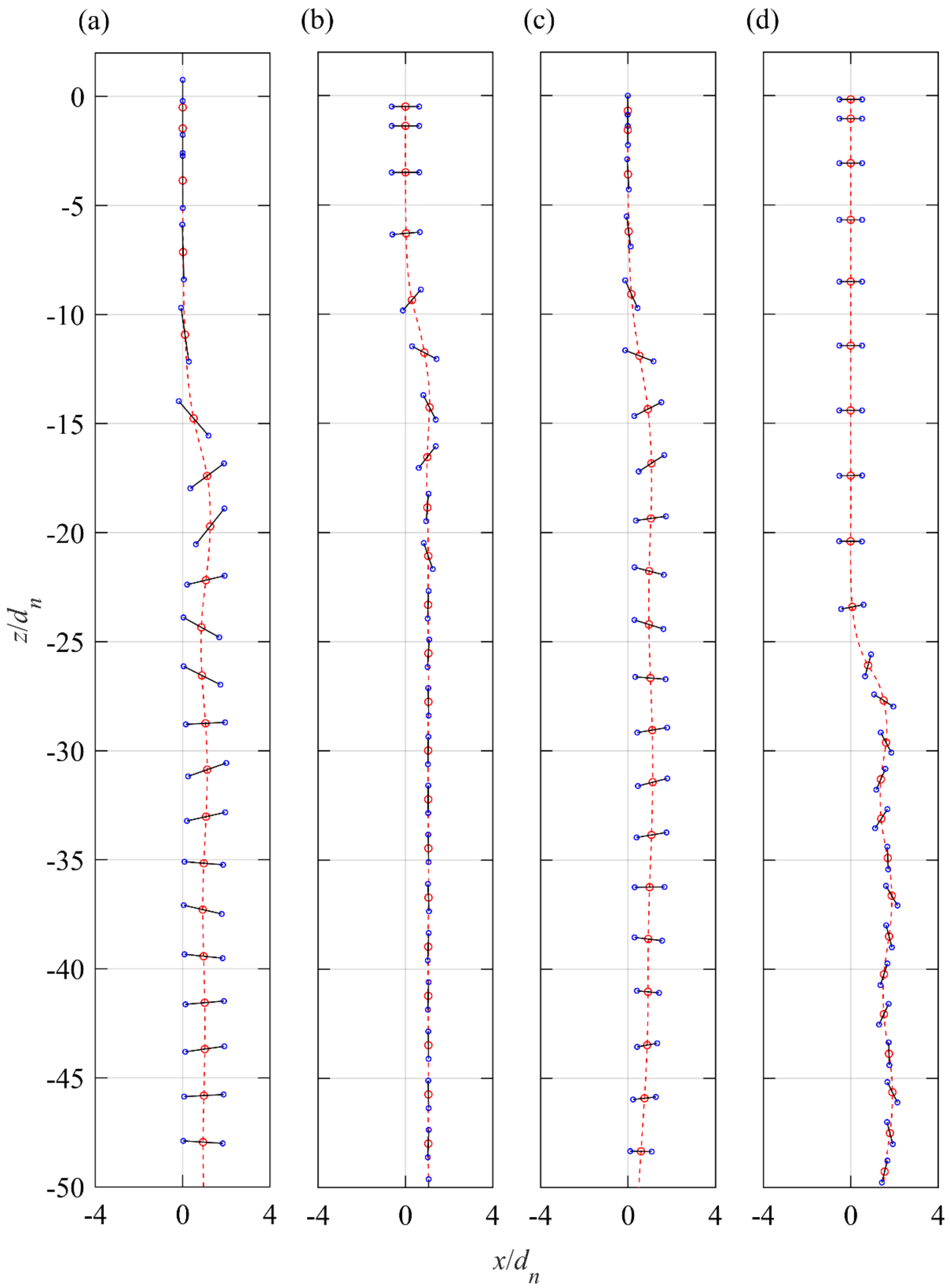

FIG. 10. Variations in settling trajectory and orientation of different particles with $d_n = 1$ mm, $\beta_0 = 90°$ and shape: (a) ellipsoid 1, (b) ellipsoid 2, (c) cylinder, and (d) disk. Red dashed line denotes the centroid trajectory, and black solid line with blue endpoints denotes the location of the revolution axis. The lengths of the revolution axes of ellipsoid 2 and the disk are doubled and tripled respectively for clarity. The time increment between each visualization is 0.02 s.

Given that gravitational force induces no torque about the mass center, torque arising from hydrodynamic forces is responsible for particle rotation. According to Mandø and Rosendahl[8], friction torque always acts to damp rotational motion, whereas torque stemming from the offset of the center of pressure from the geometric center (i.e., the mass center) accounts for particle readjustment. Figure 11 illustrates the pressure distribution around ellipsoid 1 at different instants of settling for $\beta_0 = 90°$. During the initial period, the particle moves at its initial orientation (i.e., $\beta = \beta_0 = 90°$) [Fig. 11(a)]. Although the particle experiences no torque under such circumstances, this can instinctively be interpreted as a state of unstable equilibrium. Once it experiences a certain level of disturbance, the particle starts to deviate from the state of unstable equilibrium, and the pressure distribution is no longer symmetric around the particle [Figs. 11(b) and 11(c)]. This change promotes additional torque due to the displacement of the center of pressure, thus forcing the particle to rotate. Eventually, a state of stable equilibrium is reached whereby the center of pressure is consistent with the geometric center, and the torque vanishes [Fig. 11(d)]. The terminal settling state of a particle is commonly characterized by this stable equilibrium state without regard to secondary motions like oscillation.

Based on the above description, the settling process of a non-spherical particle in the intermediate regime may be divided into three chronological stages. In Stage 1, the particle provisionally settles at an unstable equilibrium state. In Stage 2, the particle self-readjusts to the stable equilibrium state. In Stage 3, the particle progressively attains the terminal settling state where secondary motions may occur. Notably, particles with certain initial orientations may not experience Stage 1 and even Stage 2. Moreover, the settling velocity can dramatically increase in Stage 1, leading to a considerably longer vertical displacement [see Figs. 9(c) and 9(f)]. Particles with $d_n = 0.25$ mm ($Re_p \approx 10$) exhibit qualitatively similar settling behavior to those with $d_n = 1$ mm, yet appear to be oriented directly to the stable equilibrium state of $\beta = 0°$ without exhibiting oscillations in Stage 2 (Fig. 12).

As a settling particle rotates due to hydrodynamic torque, the rotational motion of the particle can in turn appreciably affect the flow field around it and may thus promote specific wake structures. Fig. 13 visualizes the flow fields around particles of different shapes with $d_n = 1$ mm and $\beta_0 = 90°$. The Ω_R method proposed by Dong et al.[48] is used for vortex identification. An iso-surface of $\Omega_R = 0.52$ is chosen to capture the vortical structures. As illustrated in Fig. 13(a), the wake of ellipsoid 1 initially consists of two thread-like vortices that are attached to the particle. As the particle rotates, instability develops, and vortex shedding occurs. The detaching vortices push the flow near and around the particle upwards, forming a low-pressure region that generates a torque on the particle in the opposite direction. This additional torque along with inertia can further lead to particle oscillations because new vortices can detach on the other side when the particle reaches the opposite inclination and so on, each time it changes orientation. Notably, the vortical structure is closely related to the particle shape. Similar to ellipsoid 1, a double-threaded wake structure is observed for the cylinder [Fig. 13(c)], whereas flatter particles like ellipsoid 2 and the disk present a so-called hairpin structure[49,50] [Figs. 13(b) and 13(d)]. Vortex shedding is less pronounced for particles with $d_n = 1$ mm and $\beta_0 = 45°$. This is mainly because the absence of Stage 1 leads to relatively low Re_p in Stage 2. For particles with $d_n = 0.25$ mm however, no vortex shedding is observed for all simulated shapes and initial orientations. The foregoing suggests that the occurrence of vortex shedding depends largely on the magnitude of Re_p. An unstable initial orientation may promote vortex shedding because larger Re_p can be reached and rotational motion is induced. In turn, vortex shedding can affect the settling motion by causing the particle to oscillate in Stage 2 and Stage 3.

Figure 14 presents contour plots of the vertical flow velocity component around particles of different shapes for $d_n = 1$ mm and $\beta_0 = 90°$. Sinuous wake structures associated with varying particle orientation can be observed. Moreover, the velocity distribution in the wake exhibits an asymmetric pattern even as the particle approaches the state of stable equilibrium [Figs. 14(a) and 14(d)]. In fact, the high-velocity zone is located close to the downward-rotating end of the particle, reflecting the effect of rotational motion on the flow field.

Overall, our results provide insight into the settling process of non-spherical particles in the intermediate regime. The initial orientation of non-spherical particles plays a key role in the settling process and so should be taken into account for particulate flows.

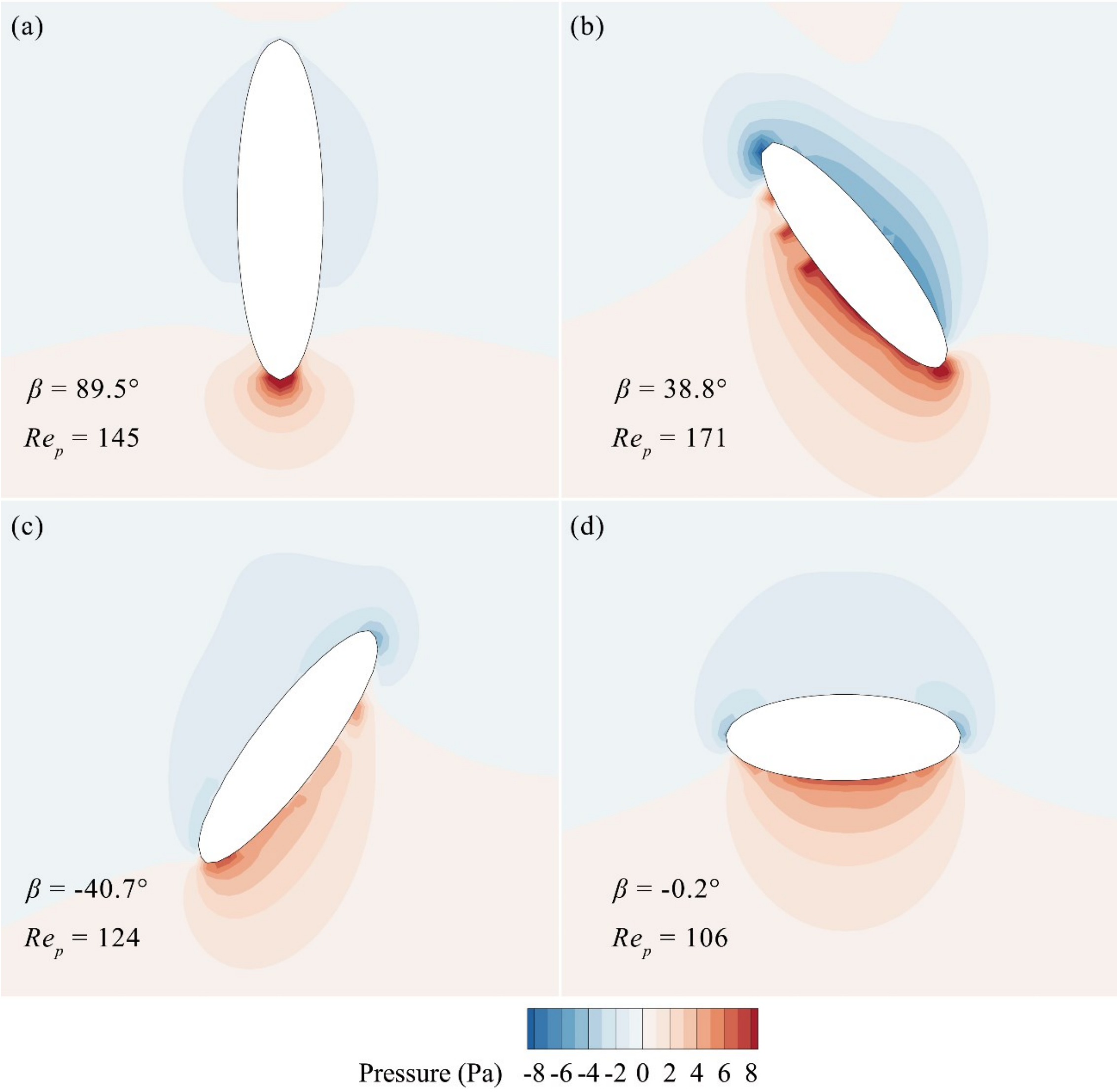

FIG. 11. Pressure distribution contours around ellipsoid 1 with $d_n = 1$ mm and $\beta_0 = 90°$ at different instants of settling: $t =$ (a) 0.04 s, (b) 0.10 s, (c) 0.14 s, and (d) 0.60 s.

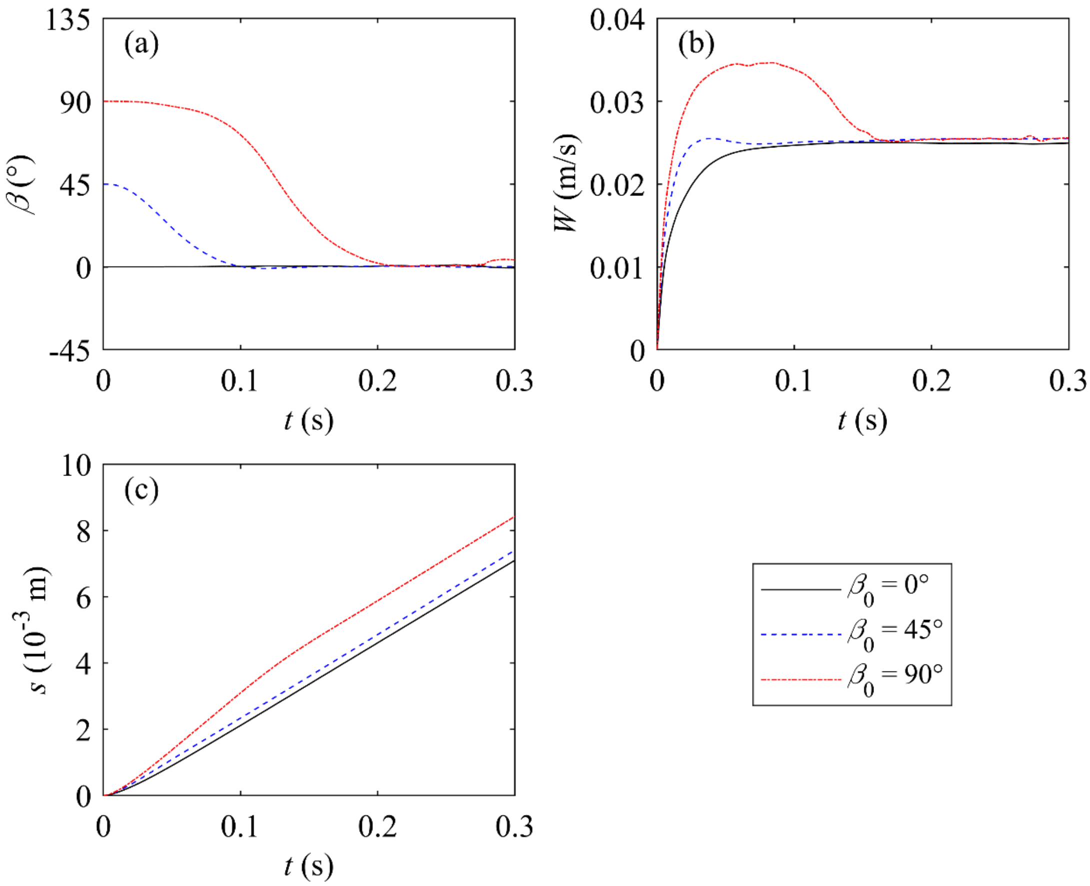

FIG. 12. Time histories of (a) orientation angle β, (b) settling velocity W, and (c) vertical displacement s for ellipsoid 1 with $d_n = 0.25$ mm.

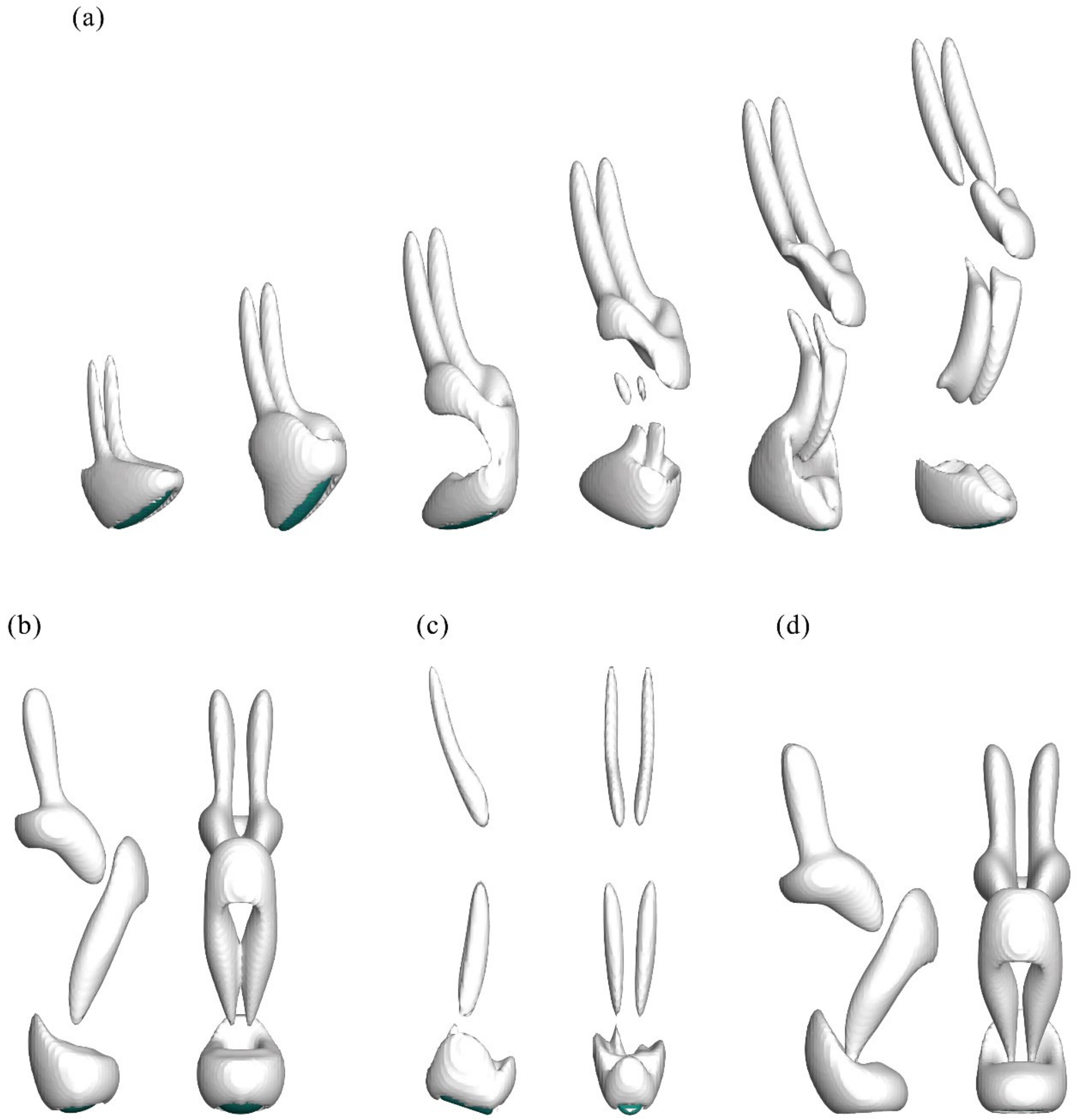

FIG. 13. Vortices in the wake of particles of different shapes for $d_n = 1\ \text{mm}$ and $\beta_0 = 90°$ during orientation readjustment: (a) ellipsoid 1, t = 0.12~0.22 s, (b) ellipsoid 2, t = 0.18 s, (c) cylinder, t = 0.20 s, and (d) disk, t = 0.30 s. An iso-surface of $\Omega_R = 0.52$ is chosen to capture vortical structures.[48]

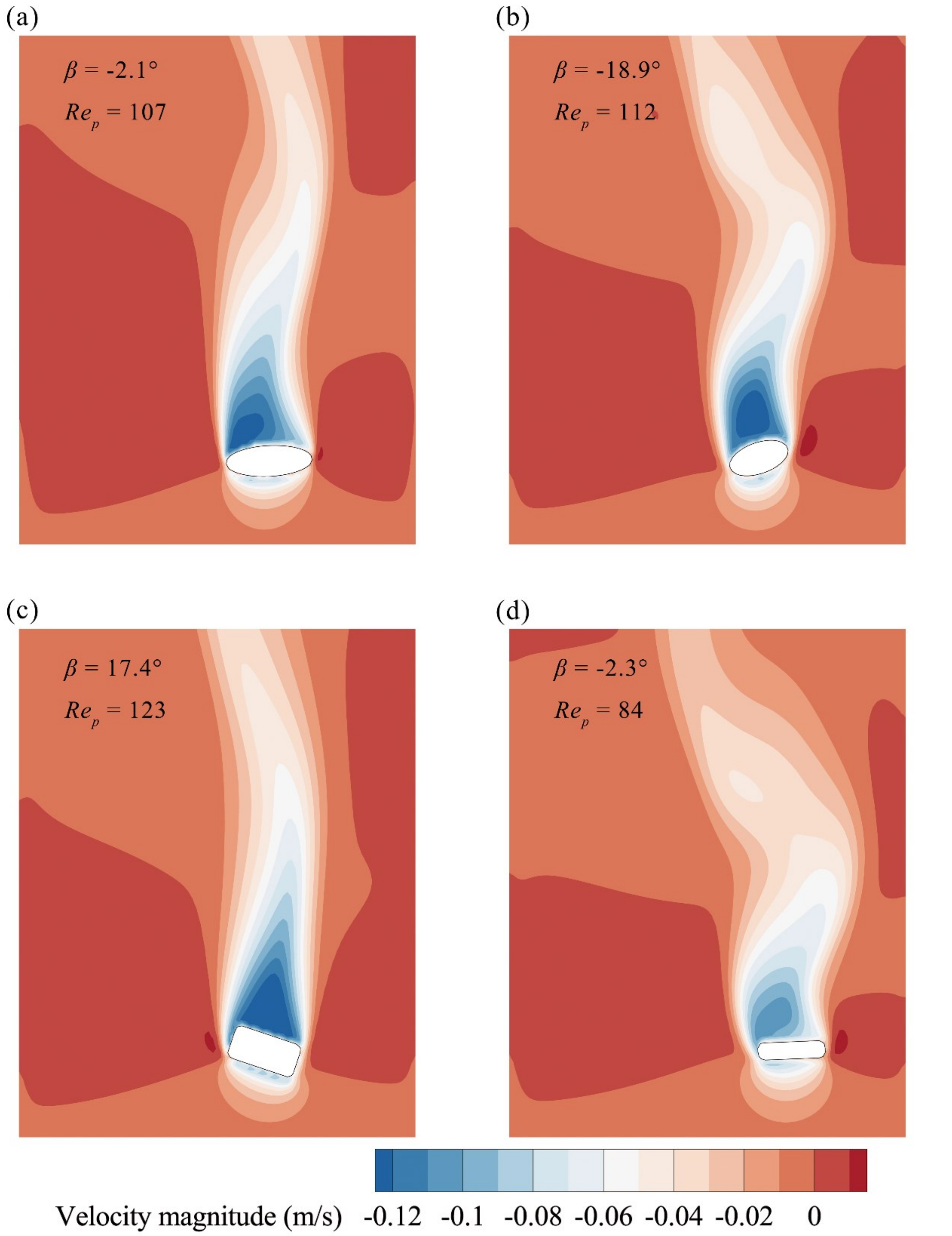

FIG. 14. Contour plots of vertical flow velocity component around particles of different shapes with $d_n = 1$ mm and $\beta_0 = 90°$ during orientation readjustment: (a) ellipsoid 1, $t = 0.22$ s, (b) ellipsoid 2, $t = 0.18$ s, (c) cylinder, $t = 0.20$ s, and (d) disk, $t = 0.30$ s.

IV. CONCLUSION

This study has investigated the effects of particle shape and initial orientation on the settling of non-spherical particles. Commercial CFD software FLOW-3D was used to perform a series of PR-DNS simulations of the settling in otherwise quiescent water of spheres and five types of regular, non-spherical sediment particles, i.e., prolate spheroid, oblate spheroid, cylinder, disk, and cube. A dual-Euler whole-attitude solver was used to reproduce particle orientation behavior. In the study, the Galileo number was varied from 0.248 to 360 with the particle Reynolds number Re_p ranging from 0.00277 to 562. Based on the computational results, the main findings are summarized as follows:

(1) A non-spherical particle experiences larger drag and consequently attains a lower terminal velocity than its spherical counterpart. For sufficiently small Re_p when the viscous force dominates, the terminal velocity is less affected by the particle shape (characterized by the particle aspect ratio). For relatively large Re_p when the inertial force becomes dominant, the shape effect becomes significant, and should be represented by the Corey shape factor. When the inertial force becomes significant or the particle shape deviates from a sphere, then pressure drag may dominate over friction drag.

(2) Empirical correlations were derived for the dimensionless characteristic time t_{95*} and dimensionless characteristic displacement s_{95*} of particle settling. It was demonstrated that t_{95*} remains constant in the Stokes regime and decreases as Re_p increases in the intermediate regime; s_{95*} increases logarithmically with increasing Re_p over the simulated range, whereas the slope in s_{95*} with

Re_p observed in the Stokes regime reduces in the intermediate regime.

(3) In the Stokes regime, the orientation of a non-spherical particle remains essentially unchanged during the settling process. A non-spherical particle with different initial orientations can attain various terminal velocities which increase with crosswise sphericity ϕ_c. The flow velocity distribution in the vicinity of a particle of any shape exhibits a highly symmetric pattern. A given particle appears to move in tandem with the surrounding fluid, such that the effect of its asymmetry is marginal.

(4) In the intermediate regime, a non-spherical particle provisionally settling at an unstable orientation tends to readjust itself to a stable equilibrium state. In general, such a particle may experience three stages during its settling process: settling provisionally at an unstable equilibrium state; self-readjusting to the stable equilibrium state; and progressively approaching the terminal state where secondary motions may occur. Due to the identical orientation attained at terminal settling, the effect of initial orientation on terminal velocity is negligible, while an unstable initial orientation can result in a longer vertical displacement and may promote vortex shedding. It is therefore important to consider the initial orientation of non-spherical particles when modeling particulate flows.

In many real-world situations, particles do not settle in isolation. Vortices induced by nearby particles can significantly influence the overall settling behavior, e.g., causing repulsion in dual-particle cases,[51] promoting clusters for monodisperse particles,[52] and altering the orientation of rod-like particles.[53] Direct inter-particle interactions (collisions) also play an important role in the dynamics of particles particularly when in a dense regime.[54,55] Therefore, we intend to carry out future research into the behavior of multiparticle systems. Moreover, the present work has provided us with a unique basis to investigate the settling of irregular particles; this work is underway.

SUPPLEMENTARY MATERIAL

The Supplementary Material provides a brief description of the dual-Euler whole-attitude solver used to model variation in particle orientation.

ACKNOWLEDGMENTS

The present work was financially supported by the National Natural Science Foundation of China (Grant No. 52239007).

AUTHOR DECLARATIONS

Conflict of Interest

The authors have no conflicts to disclose.

Author Contributions

Xiaoyong Cheng: Data curation (lead); Formal analysis (lead); Investigation (equal); Methodology (equal); Validation (lead); Visualization (lead); Writing – original draft (lead). **Zhixian Cao:** Conceptualization (equal); Funding acquisition (lead); Investigation (equal); Methodology (equal); Project administration (lead); Resources (lead);

Supervision (lead); Writing – review & editing (equal). **Ji Li:** Conceptualization (equal); Investigation (equal); Writing – review & editing (equal). **Alistair Borthwick:** Conceptualization (equal); Investigation (equal); Writing – review & editing (equal).

DATA AVAILABILITY

Data that support the findings of this study are available from the corresponding author upon reasonable request.

APPENDIX: VALIDATION OF THE CFD MODEL

The settling of a solid sphere in quiescent water was experimentally investigated by Mordant and Pinton[56] who derived the temporal variation in settling velocity from measurements of the Doppler shift of an ultrasonic wave scattered by a moving particle. Two cases with $d_n = 0.5$ mm and 1.5 mm are simulated to validate the applied CFD model. The particle density is $\rho_p = 2560$ kg/m^3, the water density is $\rho_f = 1000$ kg/m^3, and the dynamic viscosity of water $\mu = 8.9 \times 10^{-4}$ kg/m/s. The simulation setup is the same as previously described in Sec. II.B except that three mesh resolutions are tested, i.e., $\Delta h = 1/10,\ 1/12$, and $1/14\ d_n$.

Fig. 15 shows that there is good agreement between the simulated and measured settling velocities, thus validating the model, and demonstrating that a mesh resolution of $\Delta h = 1/12 d_n$ is sufficiently fine to produce accurate results.

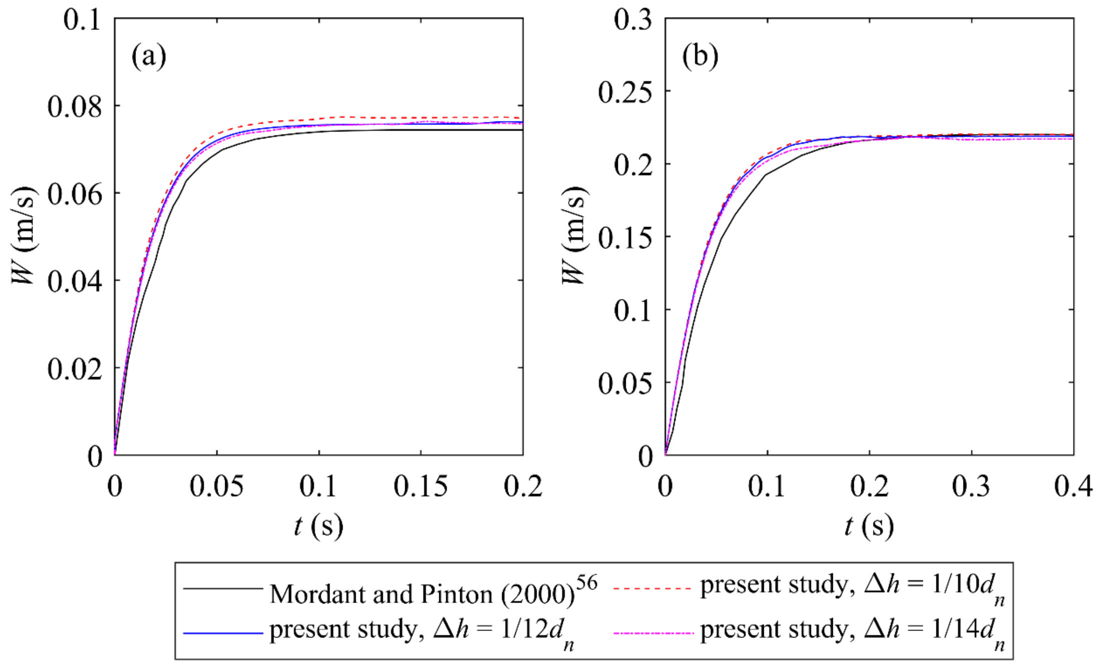

FIG. 15. Time history of settling velocity W for spheres of (a) $d_n = 0.5$ mm and (b) $d_n = 1.5$ mm. Black solid line refers to measured data by Mordant and Pinton[56].

REFERENCES

[1]M. Church, "Bed material transport and the morphology of alluvial river channels," Annu. Rev. Earth Planet. Sci. **34**(1), 325-354 (2006).

[2]S. Dey, A. S. Zeeshan, and E. Padhi, "Terminal fall velocity: the legacy of Stokes from the perspective of fluvial hydraulics," Proceedings of the Royal Society A **475**(2228), 20190277 (2019).

[3]I. A. Kane and M. A. Clare, "Dispersion, accumulation, and the ultimate fate of microplastics in deep-marine environments: A review and future directions," Front. Earth Sci. **7**, 00080 (2019).

[4]J. Li, E. Shan, J. Zhao, J. Teng, and Q. Wang, "The factors influencing the vertical transport of microplastics in marine environment: A review," Sci. Total Environ. **870**,

161893 (2023).

[5]B. R. Barboza, B. Chen, and C. Li, “A review on proppant transport modelling,” J. Pet. Sci. Eng. **204**, 108753 (2021).

[6]S. Yao, C. Chang, K. Hai, H. Huang, and H. Li, “A review of experimental studies on the proppant settling in hydraulic fractures,” J. Pet. Sci. Eng. **208**, 109211 (2022).

[7]R. P. Chhabra and J. F. Richardson, *Non-Newtonian Flow and Applied Rheology: Engineering Applications* (Butterworth-Heinemann, 2008).

[8]M. Mandø and L. Rosendahl, “On the motion of non-spherical particles at high Reynolds number,” Powder Technol. **202**, 1-13 (2010).

[9]H. Ma, L. Zhou, Z. Liu, M. Chen, X. Xia, and Y. Zhao, “A review of recent development for the CFD-DEM investigations of non-spherical particles,” Powder Technol. **412**, 117972 (2022).

[10]Y. Zhao, P. Zhang, L. Lei, L. Kong, S. A. Galindo-Torres, and S. Z. Li, “Metaball-Imaging discrete element lattice Boltzmann method for fluid–particle system of complex morphologies with case studies,” Phys. Fluids **35**(2), 023308 (2023).

[11]R. Clift and W. H. Gauvin, “Motion of entrained particles in gas streams,” Can. J. Chem. Eng. **49**(4), 439-448 (1971).

[12]N. Cheng, “Comparison of formulas for drag coefficient and settling velocity of spherical particles,” Powder Technol. **189**(3), 395-398 (2009).

[13]A. Terfous, A. Hazzab, and A. Ghenaim, “Predicting the drag coefficient and settling velocity of spherical particles,” Powder Technol. **239**, 12-20 (2013).

[14]W. E. Dietrich, “Settling velocity of natural particles,” Water Resour. Res. **18**(6), 1615-1626 (1982).

[15]A. Haider and O. Levenspiel, “Drag coefficient and terminal velocity of spherical and nonspherical particles,” Powder Technol. **58**(1), 63-70 (1989).

[16]A. Hölzer and M. Sommerfeld, "New simple correlation formula for the drag coefficient of non-spherical particles," Powder Technol. **184**(3), 361-365 (2008).

[17]F. Dioguardi and D. Mele, "A new shape dependent drag correlation formula for non-spherical rough particles. Experiments and results," Powder Technol. **277**, 222-230 (2015).

[18]G. Bagheri and C. Bonadonna, "On the drag of freely falling non-spherical particles," Powder Technol. **301**, 526-544 (2016).

[19]A. T. Corey, "Influence of shape on the fall velocity of sand grains," Ph.D. thesis (Colorado State University, 1949).

[20]B. J. Connolly, E. Loth, and C. F. Smith, "Shape and drag of irregular angular particles and test dust," Powder Technol. **363**, 275-285 (2020).

[21]Y. Li, Q. Yu, S. Gao, and B. W. Flemming, "Settling velocity and drag coefficient of platy shell fragments," Sedimentology **67**(4), 2095-2110 (2020).

[22]S. Chien, "Settling velocity of irregularly shaped particles," SPE Drill. Complet. **9**(04), 281-289 (1994).

[23]X. Song, Z. Xu, G. Li, Z. Pang, and Z. Zhu, "A new model for predicting drag coefficient and settling velocity of spherical and non-spherical particle in Newtonian fluid," Powder Technol. **321**, 242-250 (2017).

[24]R. Büttner, P. Dellino, L. La Volpe, V. Lorenz, and B. Zimanowski, "Thermohydraulic explosions in phreatomagmatic eruptions as evidenced by the comparison between pyroclasts and products from Molten Fuel Coolant Interaction experiments," Journal of Geophysical Research: Solid Earth **107**(B11), ECV 5-1-ECV 5-14 (2002).

[25]P. Dellino, D. Mele, R. Bonasia, G. Braia, L. La Volpe, and R. Sulpizio, "The analysis of the influence of pumice shape on its terminal velocity," Geophys. Res. Lett. **32**(21) (2005).

[26]Y. Wang, L. Zhou, Y. Wu, and Q. Yang, "New simple correlation formula for the drag coefficient of calcareous sand particles of highly irregular shape," Powder Technol. **326**, 379-392 (2018).

[27]R. Clift, J. R. Grace, and M. E. Weber, *Bubbles, Drops, and Particles* (Academic Press, New York, 1978).

[28]E. Loth, "Drag of non-spherical solid particles of regular and irregular shape," Powder Technol. **182**(3), 342-353 (2008).

[29]M. de Kruijf, A. Slootman, R. A. de Boer, and J. J. G. Reijmer, "On the settling of marine carbonate grains: Review and challenges," Earth-Sci. Rev. **217**, 103532 (2021).

[30]M. Zastawny, G. Mallouppas, F. Zhao, and B. van Wachem, "Derivation of drag and lift force and torque coefficients for non-spherical particles in flows," Int. J. Multiph. Flow **39**, 227-239 (2012).

[31]R. Ouchene, M. Khalij, B. Arcen, and A. Tanière, "A new set of correlations of drag, lift and torque coefficients for non-spherical particles and large Reynolds numbers," Powder Technol. **303**, 33-43 (2016).

[32]S. K. P. Sanjeevi, J. A. M. Kuipers, and J. T. Padding, "Drag, lift and torque correlations for non-spherical particles from Stokes limit to high Reynolds numbers," Int. J. Multiph. Flow **106**, 325-337 (2018).

[33]R. Ouchene, "Numerical simulation and modeling of the hydrodynamic forces and torque acting on individual oblate spheroids," Phys. Fluids **32**(7), 073303 (2020).

[34]F. Carranza and Y. Zhang, "Study of drag and orientation of regular particles using stereo vision, Schlieren photography and digital image processing," Powder Technol. **311**, 185-199 (2017).

[35]H. Başağaoğlu, S. Succi, D. Wyrick, and J. Blount, "Particle shape influences settling and sorting behavior in microfluidic domains," Sci. Rep. **8**(1) (2018).

[36]S. Ghosh and P. Yadav, "Study of gravitational settling of single semi-torus shaped particle using immersed boundary method," Appl. Math. Comput. **413**, 126643 (2022).

[37]D. Hui, Z. Xu, G. Zhang, and M. Liu, "Sedimentation of elliptical particles in Bingham fluids using graphics processing unit accelerated immersed boundary-lattice Boltzmann method," Phys. Fluids **35**(1), 13330 (2023).

[38]C. W. Hirt and J. M. Sicilian, "A porosity technique for the definition of obstacles in rectangular cell meshes," in *International Conference on Numerical Ship Hydrodynamics, 4th*, Washington, DC (1985).

[39]F. Xiao, "A Computational Model for Suspended Large Rigid Bodies in 3D Unsteady Viscous Flows," J. Comput. Phys. **155**(2), 348-379 (1999).

[40]C. P. Tsai, Y. C. Chen, T. O. Sihombing, and C. Lin, "Simulations of moving effect of coastal vegetation on tsunami damping," Nat. Hazards Earth Syst. Sci. **17**(5), 693-702 (2017).

[41]A. Kermanpur, S. Mahmoudi, and A. Hajipour, "Numerical simulation of metal flow and solidification in the multi-cavity casting moulds of automotive components," J. Mater. Process. Technol. **206**(1-3), 62-68 (2008).

[42]X. Zhu, Y. H. Zeng, and W. X. Huai, "Settling velocity of non-spherical hydrochorous seeds," Adv. Water Resour. **103**, 99-107 (2017).

[43]G. H. Bagheri, C. Bonadonna, I. Manzella, and P. Vonlanthen, "On the characterization of size and shape of irregular particles," Powder Technol. 270, 141-153 (2015).

[44]J. Guo, "Motion of spheres falling through fluids," J. Hydraul. Res. **49**(1), 32-41 (2011).

[45]W. W. Rubey, "Settling velocity of gravel, sand, and silt particles," Am. J. Sci. **s5-25**(148), 325-338 (1933).

[46]J. Guo, "Logarithmic matching and its applications in computational hydraulics and sediment transport," J. Hydraul. Res. **40**(5), 555-565 (2002).

[47]G. E. Stringham, D. B. Simons, and H. P. Guy, *The Behavior of Large Particles Falling in Quiescent Liquids* (US Government Printing Office, 1969).

[48]X. Dong, Y. Gao, and C. Liu, "New normalized Rortex/vortex identification method," Phys. Fluids **31**(1), 011701 (2019).

[49]H. Zhong, S. Chen, and C. Lee, "Experimental study of freely falling thin disks: Transition from planar zigzag to spiral," Phys. Fluids **23**(1), 011702 (2011).

[50]M. N. Ardekani, P. Costa, W. P. Breugem, and L. Brandt, "Numerical study of the settling of spheroidal particles," Int. J. Multiph. Flow **87**, 16-34 (2016).

[51]J. Liu, P. Zhang, Y. Xiao, Z. Wang, S. Yuan, and H. Tang, "Interaction between dual spherical particles during settling in fluid," Phys. Fluids **33**(1), 013312 (2021).

[52]A. A. Zaidi, "Settling characteristics of bidisperse dilute suspension in the vortex shedding regime," Phys. Fluids **32**(9), 093310 (2020).

[53]A. Hamid, A. B. Arshad, S. Mehdi, M. D. Qasim, A. Ullah, J. J. Molina, and R. Yamamoto, "A numerical study of sedimentation of rod like particles using smooth profile method," Int. J. Multiph. Flow **127**, 103263 (2020).

[54]A. Esteghamatian, A. Hammouti, M. Lance, and A. Wachs, "Particle resolved simulations of liquid/solid and gas/solid fluidized beds," Phys. Fluids **29**(3), 033302 (2017).

[55]Y. Yao, C. S. Criddle, and O. B. Fringer, "The effects of particle clustering on hindered settling in high-concentration particle suspensions," J. Fluid Mech. **920**, A40 (2021).

[56]N. Mordant and J. F. Pinton, "Velocity measurement of a settling sphere," Eur. Phys. J. B **18**(2), 343-352 (2000).